Strong coupling effect in the elastic scattering of the ^{10}C+^{58}Ni system near barrier

V. Guimarães, E. N. Cardozo, V. B. Scarduelli, J. Lubian, J. J. Kolata, P. D. O'Malley, D. W. Bardayan, E. F. Aguilera, E. Martinez-Quiroz, D. Lizcano, A. Garcia-Flores, M. Febbraro, C. C. Lawrence, J. Riggins, R. O. Torres-Isea, P. N. de Faria, D. S. Monteiro, E. S. Rossi, Jr., and N. N. Deshmukh

Phys. Rev. C **100**, 034603 — Published 3 September 2019

DOI: 10.1103/PhysRevC.100.034603

Strong coupling effect in the elastic scattering of the ^{10}C+^{58}Ni system near barrier.

V. Guimarães[1], E. N. Cardozo[1,2], V. B. Scarduelli[1], J. Lubian[2], J. J. Kolata[3], P. D. O'Malley[3], D. W. Bardayan[3], E. F. Aguilera[4], E. Martinez-Quiroz[4], D. Lizcano[4], A. Garcia-Flores[4], M. Febbraro[5], C. C. Lawrence[6], J. Riggins[7], R. O. Torres-Isea[7], P. N. de Faria[2], D. S. Monteiro[8], E. S. Rossi Jr[1], N. N. Deshmukh[9]

1) Instituto de Física,
Universidade de São Paulo,
Rua do Matão, 1371,
São Paulo 05508-090, SP, Brazil
2) Instituto de Física,
Universidade Federal Fluminense,
Avenida Litorânea s/n, Gragoatá,
Niterói, 24210-340 RJ, Brazil
3) Physics Department,
University of Notre Dame,
Notre Dame, Indiana, 46556-5670, USA
4) Departamento de Aceleradores,
Instituto Nacional de Investigaciones Nucleares,
Apartado Postal 18-1027,
Código Postal 11801, México,
Distrito Federal, México.
5) Physics Division,
Oak Ridge National Laboratory,
Oak Ridge, TN 37381
6) Kennedy School of Government,
Harvard University,
Cambridge, MA 02138.
7) Physics Department,

University of Michigan,
Ann Arbor, Michigan 48109, USA
8) Universidade Federal da Integração Latino-Americana,
Instituto Latino-Americano de Ciências da Vida e da Natureza,
Foz do Iguaçú, PR, Brazil
9) Nuclear Physics Division,
Saha Institute of Nuclear Physics,
Kolkata, India

(Dated: July 26, 2019)

Abstract

The elastic scattering of the radioactive proton-rich carbon isotope, ^{10}C, has been investigated. A full differential angular distribution for the elastic scattering of ^{10}C on a ^{58}Ni target has been measured at $\mathrm{E_{Lab}} = 35.3$ MeV, which is just above the Coulomb Barrier for this system ($\mathrm{V_B} = 27$ MeV). The obtained angular distribution was analyzed in terms of coupled channel (CC), coupled reaction channel (CRC) and continuum discretized coupled channel (CDCC) calculations. In the coupled-channel calculation, several inelastic transitions of the target and the first (2^+) excited state of the ^{10}C projectile were considered. The coupling to the first (2^+) excited state of ^{10}C was shown to be very important to describe the rising of the cross section at backward angles. We also performed an analysis with the continuum discretized coupled channels, considering the ^{9}B+p and ^{6}Be+α channels, which indicated a strong cluster configuration for the ^{10}C projectile.

PACS numbers: 25.70.Bc, 24.10.Eq

I. INTRODUCTION

Elastic scattering has often been used to investigate static and dynamics effects of the projectile interaction on medium-mass and heavy targets [1, 2]. Due to its high cross section, when compared with other direct reactions, the elastic scattering process has been used to investigate the structure of light radioactive ion projectiles [3]. The description of the cross sections for elastic scattering is very sensitive to the interaction potential between the projectile and target nuclei and to the structure of the nuclei involved. Some of the light radioactive nuclei are weakly bound and some of them can exhibit exotic structures, such as halo structure [4]. Elastic scattering induced by exotic neutron-rich nuclei, at energies close to the barrier, has shown interesting and intriguing coupling effects. In particular, elastic scattering induced by the ^{6}He and ^{11}Li nuclei, which have a peculiar structure formed by ^{4}He and ^{9}Li cores, respectively, surrounded by two-neutron valence particles forming a halo of rarefied nuclear matter, has shown the importance of the coupling to the continuum in the description of the elastic scattering data (see for instance refs. [5–11]). For ^{11}Li, the coupling effect is quite strong due to the much stronger Coulomb dipole polarisability of this nucleus [11, 12]. For these light neutron-rich nuclei, the coupling effect due to the Coulomb dipole is observed in the angular distribution of the elastic scattering by damping of the Fresnel peak (nuclear-Coulomb interference peak). The strong damping of the Fresnel peak is also seen in the angular distribution data for the ^{11}Be+^{64}Zn system, where, in this case, the damping is due to the strong nuclear couplings to the low-lying ^{10}Be+n states [13–15]. A review on the effects of strong coupling in elastic scattering can be found in Ref. [16]. Data on elastic scattering induced by proton-rich nuclei at energies close to the barrier are quite scarce. Although less probable, proton-halos are also possible and one such case is the ^{8}B nucleus [17, 18]. The low separation energy of the proton valence particle in this projectile (S_p=0.138 MeV) produces a decoupling between the valence particle and the core during the interaction with a target and the breakup process becomes an important competing mechanism even at relatively low incident energies. Elastic scattering of the radioactive weakly-bound and proton-rich ^{8}B projectile on a ^{58}Ni target has been investigated at energies close to the barrier and the coupling to the ^{7}Be+p breakup channel has been shown to be crucial to describe the data [19–21]. For heavier targets such as ^{208}Pb the angular distribution of ^{8}B elastic scattering, at energies three times the barrier, shows a classic Fresnel scattering pattern [22]. However, calculations for the same target but at energies close to the barrier suggests a suppression of the Fresnel peak due to the halo structure of ^{8}B and couplings to states in the continuum [23]. These experiments have shown the importance of the cluster configuration and halo structure of some light nuclei, which strongly influences the reaction dynamics at energies close to the barrier. Although some advances have been achieved in the understanding of the nuclear interaction induced by these weakly-bound and/or exotic nuclei, the precise description of the influence of the breakup and dynamic effects is still not completely known. In this sense, more data on elastic scattering induced by some other proton-rich nuclei such as ^{9}C, ^{10}C, ^{12}N and ^{13}O, at energies close to the barrier, would be highly desirable and very welcome.

Quasi-elastic scattering data for the ^{10}C+^{208}Pb system at energies of three times the Coulomb barrier [24], as well as for the ^{10}C+^{27}Al system at two times the barrier [25], have been reported in the literature. For both cases, there is no evidence of strong couplings. Here we report on the investigation of the elastic scattering of the proton-rich nucleus ^{10}C on a ^{58}Ni target at E_{Lab}= 35.3 MeV (E_{cm}= 30.0 MeV), which is close to the barrier (V_{B}= 27.0 MeV). The proton-rich carbon isotope ^{10}C, whose ground-state has $J^{\pi} = 0^{+}$, is an interesting nucleus. It decays by three possible channels: ^{8}Be+2p, ^{9}B+p and ^{6}Be+α, with binding energies of 3.820 MeV, 4.006 MeV and 5.101 MeV, respectively. Since the residual ^{8}Be, ^{9}B and ^{6}Be nuclei are also unbound by proton or *alpha* particle decays, this nucleus can be considered to have a 4-body configuration: $\alpha - \alpha - p - p$. After removing any one of these particles, the remaining nucleus also breaks apart. Due to this 4-body configuration, ^{10}C is the only nucleus supposed to have a Brunnian (super-borromean) structure [26], where the four interactions of the constituent particles can be associated with four interconnected rings. This exotic configuration has been investigated in the past at the GANIL laboratory in an breakup experiment [27], where protons and alphas were detected in coincidence. The measured angular distribution was analyzed with coupled channel (CC) calculations, where projectile and target inelastic channels, as well as reorientation, were included in the coupling matrix. Also, coupled reaction channel (CRC) and continuum discretized coupled channel (CDCC) calculations were performed.

The present paper is organized as follows. Section II contains a description of the experiment. Section III presents the data and gives the results of the coupled channels (CC) calculations. Section IV is dedicated to the coupled reaction channel (CRC) analysis, while

Section V is devoted to the description of the continuum discretized coupled channel (CDCC) calculations. Finally, last section presents a summary of this work.

II. EXPERIMENTAL SETUP AND MEASUREMENTS

The angular distribution for elastic scattering of ^{10}C on ^{58}Ni was measured at $E_{\rm Lab}$=35.3 MeV. The secondary ^{10}C radioactive ion beam was produced by the *Twinsol* system [28, 29] installed at the Nuclear Science Laboratory of the University of Notre Dame, USA. This system consists of two superconducting solenoids with 6.0 T maximum central field and a 30 cm clear warm bore. The ^{10}C secondary radioactive beam was produced in-flight with the ^{3}He(^{10}B,^{10}C) ($Q_{\rm value}$=-3.670 MeV) charge-exchange reaction. The production target consisted of a gas cell filled with ^{3}He gas up to 0.5 atm and sealed with Ti foils 2.0μm thick. The gas target was mounted in a chamber just before the first solenoid. The ^{10}B^{5+} primary beam was accelerated to an energy of 54.0 MeV, and had an intensity of typically 200 enA. It was collected after the production target by a Faraday cup, which stops all particles in the angular range from 0° to 2.7° and integrates the charge. The two solenoids in the *Twinsol* system act as thick lenses to collect, select and focus the secondary beam, produced in the forward direction ($2.7^\circ \leq \theta_{\rm Lab} \leq 6.0^\circ$), into a scattering chamber. A system of blocks and collimators located downstream in the beam line is used to clean up the beam of interest. The selection of the beam is given by the magnetic rigidity, $(B\rho)^2 \approx EA/Q^2$, where B is the magnetic field, E, A and Q are the energy, mass and charge state of the beam. The magnetic field is adjusted to optmize the yield of the beam of interest. For this experiment, the ^{10}C beam was produced and focused not in the ground-state but at its first excited state at E^*=3.354 MeV. The ^{10}C ground-state has J^π=0^+ and $T_{1/2}$=19.3 s while the only bound excited state has $J^\pi = 2^+$ and $T_{1/2}$=107 fs. This procedure avoids the ^{11}C contamination. In an attempt to produce ^{10}C beam in the ground-state, we noticed the presence of ^{11}C*(6.478 MeV), also produced in the target with about same intensity and magnetic rigidity as ^{10}C$_{g.s.}$. Since the product of the energy and mass ($E \times A$) for these two particles were very similar they could barely be separated by the solenoids. To avoid the ^{11}C contamination we produced and focused the ^{10}C* at an excitation energy of E^*=3.354 MeV, so that the ^{11}C* is produced at excitation energy $E \approx 9.0$ MeV. At this much higher excitation energy, the ^{11}C is unbound and would not reach to the target position. Due to the short lifetime of the excited state, the ^{10}C reaches the target in its ground-state but with the advantage of no contamination of ^{11}C. The obtained intensity of the ^{10}C produced in its first excited state was $2{\times}10^5$ pps for 1μA of the primary beam.

The target used in this measurement consisted of an isotopically enriched (greater than 99%) ^{58}Ni foil 0.75 mg/cm^2 thick. This foil was mounted in a target holder together with a thin gold target, 2.0 mg/cm^2 thick, which was used, in separate runs, to obtain the overall normalization, since gold elastic scattering at these energies is expected to be Rutherford for the angular range measured. The target was rotated by 65^0 degree in the beam direction to allow for the measurement at 90°.

The detection setup for this experiment consisted of three $\mathit{\Delta}E - E$ telescopes with silicon planar detectors of 20 and 1000-μm in thickness, for the measurements at forward angles ($\theta_{\mathrm{Lab}} = 30°$, 45° and 75°), and four 1000-μm thick E planar silicon detector for measurements at backward angles ($\theta_{\mathrm{Lab}} = 90°$, 105°, 120° and 135°). The forward angles telescopes had a circular aperture that subtended a solid angle of about 3 msr, while the planar E detectors had a solid angle of about 8 msr. A picture of the detection setup can be seen in Fig. 1.

The magnetic field of the solenoid was adjusted to focus the ^{10}C secondary beam, and blocks and collimators were used to prevent particles with different magnetic rigidity from reaching the secondary target. However some contaminants, with the same magnetic rigidity as the beam of interest, such as ^{12}N, ^{10}B, ^{9}Be, ^{6}Li and ^{4}He, were also present in the beam. These particles could be identified and separated by the combination of $\mathit{\Delta}E$ and $E_{residual}$ signals from the telescopes. $\mathit{\Delta}E \times E_{\mathrm{total}}$, A particle identification spectrum, $\mathit{\Delta}E \times E_{total}$, where $E_{total} = \mathit{\Delta}E + E_{residual}$, taken at 30° with ^{58}N target, is shown in Fig. 2. In this plot, ^{10}C and the contaminant particles scattered on the nickel target are displayed and, as can be seen, they are clearly separated and identified. A typical total energy spectrum from the telescope at 30° and from the E detector at 90° can be seen in Fig. 3. The peak corresponding to ^{10}C is also identified. There is a small background present underneath the ^{10}C peak due to the higher energy ^{12}N particles but it could be estimated to obtain the correct yields. The experimental resolution for the ^{10}C beam was about 1.0 MeV, obtained from the FWHM (full width of half maximum) of the peak of the direct beam observed in a $\Delta E - E$ telescope at 0°.

The cross sections for the angular distribution were measured at $\theta_{\mathrm{Lab}} = 30°$, 45°, 75°, 90° 105°, 120° and 135°. The uncertainties in the cross sections are due to the statistical error and ranged from 2% to 50% starting from most forward to most backward angles. The cross section for the two most backward angles are very small, 15.3 mb/sr and 7.5 mb/sr and the obtained yields for the scattered ^{10}C particles were therefore small and with larger error bars. However, measurement at these backward angles is very important since the surface nuclear effects are more relevant and sensitive at these angles. Also, cross-sections measurements around 65° (center of mass framework) would be very desirable to better investigate the Fresnel diffraction peak in the angular distribution for this system.

III. COUPLED-CHANNELS CALCULATIONS

The measured angular distribution was analyzed in terms of coupled-channels (CC) calculations performed with the code FRESCO [30]. In this approach, the interaction of the beam and the target is described by a complex potential. For the real part of the potential we adopted the double-folding São Paulo potential (SPP) [31]. It can be considered as a bare potential which can take into account the nuclear interaction between the projectile and target nuclei. The relevant feature of this potential for the calculations is its double-folding characteristic. A short-range imaginary potential was considered for the imaginary part of the complex potential. This short range potential is necessary to simulate the absorption of flux due to fusion, since this channel is not explicitly included in the calculation. This short-range potential had a Woods-Saxon shape with the parameters: W=50 MeV, r_w=1.06 fm, and a_w=0.2 fm, where r_w is the reduced radius which should be multiplied by the mass term $(A_P^{1/3} + A_T^{1/3})$ to give the actual radius of the potential, and a_w is the diffuseness parameter. A_P and A_T are the mass numbers of projectile and target, respectively. This set of parameters was used in several recent previous works on elastic scattering of boron isotopes on a ^{58}Ni target [32–34]. Actually, the final results are not very sensitive to this particular choice of parameters. In the present analysis, no imaginary surface potential has been applied and the absorption from the elastic channel is introduced via the process of opening inelastic channels. In our coupled-channels calculation, all the relevant reaction channels are explicitly taken into account to describe the data.

The first channels to be investigated were the inelastic channels and the interference between them. For the present system, we considered only the first excited state of ^{10}C (J^π=2^+) at E^*=3.354 MeV, which is the only bound excited state of the projectile, and the excited states of the ^{58}Ni target up to 3.5 MeV. The spin, parity and energy of these states included in the calculation for both the ^{10}C projectile and the ^{58}Ni target were obtained from the NNDC [35] database and are listed in Table I. The $B(E2)$ value of ^{10}C was obtained from Ref. [36] and is listed in Table II. The $B(E2)$ values for ^{58}Ni states are listed in Table III while the $B(E3)$ value for the state at 4.475 MeV in ^{58}Ni is presented in Table IV. In the present CC calculation, the excited states of the projectile and target were considered to be collective in nature, and the transitions with no change in parity were calculated within the vibrational model. A comparison of the results of this calculation with the data is shown in Fig. 4. In this figure the dashed black line is the one-channel calculation (no-coupling); the red dotted line represents the results when coupling all states of the ^{58}Ni target and the purple dotted-dashed line corresponds to the calculation where the 2^+ excited state of the ^{10}C projectile is included. As can be observed in the figure, the effect of the couplings of the ^{58}Ni states is not strong but the effect of the inclusion of the 2^+ excited state of ^{10}C is considerable. The combination of all the inelastic channels does not reproduce the data though it does reduce the cross sections at the Fresnel peak and increase the elastic cross sections at backward angles.

To improve the agreement between the calculation and the data we included the spin reorientation, which is an important effect for non-zero spin and/or deformed nuclei. The spin reorientation was an important ingredient to describe the elastic scattering of ^{10,11}B+^{58}Ni [33, 34]. Here, since the ^{10}C$_{g.s.}$ has $J^{\pi} = 0^+$, we considered the spin reorientation only for the first excited state (2^+) of ^{10}C and ^{58}Ni in the coupling matrix. The corresponding reorientation parameters are indicated in Table IV. The result of the CC calculations with the inclusion of reorientation is shown in Fig. 4 by the solid blue line. As can be seen in the figure, the inclusion of spin reorientations is very important and improved considerably the agreement of the calculations with the data.

IV. COUPLED REACTION CHANNELS (CRC) CALCULATIONS

From the analysis presented in the previous section, it is clear that inelastic channels and spin reorientation were important but not totally sufficient to describe the experimental elastic data at 35.3 MeV. This is an indication that other channels such as transfer and/or breakup reactions may be important for the coupling scheme. To investigate the importance of transfer channels we considered the one-proton stripping (^{58}Ni(^{10}C,^{9}B)^{59}Cu), one-neutron pickup (^{58}Ni(^{10}C,^{11}C)^{57}Ni) and two-neutron (direct) (^{58}Ni(^{10}C,^{12}C)^{56}Ni) transfer reactions, which are channels with low-mass transfer particles having $Q_{\rm value}$ = -0.588 MeV, +0.904 MeV and +9.378 MeV, respectively. To take into account these transfer reactions we have to consider exact finite range coupled reaction channel (CRC) calculations. For this purpose, the double-folding São Paulo potential (SPP) [31] was used for the real part of the optical potential in the entrance partition, and a Woods-Saxon shape potential with depth, radius and diffuseness given by W=50 MeV, r_w=1.06 fm, and a_w=0.2 fm, was used for the imaginary part. This imaginary potential is the same one used in the previous section for the coupled channel calculations. In the outgoing partition, the imaginary part was assumed to have the same radial dependence as the real part, but multiplied by a strength coefficient N$_I$=0.78, since no couplings were explicitly considered. The single-particle wave functions were generated by considering Woods-Saxon form-factors with reduced radii and diffuseness 1.25 fm and 0.65 fm, respectively, for ^{9}B, ^{11}C, ^{12}C, ^{56}Ni, ^{57}Ni and ^{59}Cu. The depths of the Woods-Saxon potentials were varied to reproduce the experimental binding energies for one-neutron, two-neutron and one proton transfer.

The full complex remnant in the coupling matrix elements, with prior representation and nonorthogonality corrections, were adopted in the full CRC calculations, also performed with the code Fresco [30]. The overlap schemes for the one-neutron, two-neutron and one-proton transfer channels, considered in the present CRC calculations, are shown in Figs. 5, 6 and 7, respectively.

For the one- and two-neutron transfers, we calculated the spectroscopic amplitudes using the NuShellX code [37]. The *psdpn* model space and *psdmod* effective phenomenological interaction [38] were used for the projectile overlaps, for which the $1p_{1/2}$, $1p_{3/2}$, $1d_{3/2}$, $1d_{5/2}$ and $2s_{1/2}$ orbitals valence are open for neutrons and protons. ^{4}He is assumed to be a closed core. For the target overlaps, the *bjuff* model space with the *48Cauff* effective phenomenological interaction [39] was used. This model space has a ^{48}Ca nucleus as a closed core, and the $2p_{3/2}$, $1f_{5/2}$, $2p_{1/2}$, and $1g_{9/2}$ as valence orbitals for neutrons together with $1f_{7/2}$ and $2p_{3/2}$ for protons. The spectroscopic amplitudes for one-neutron transfer are listed in Table VI, and those for two-neutrons transfer are listed in Table IX. Using these amplitudes, CRC calculations for one- and two-neutrons transfer were performed. The results can be seen in Fig. 8, which shows that these transfer channels have little influence on the elastic scattering cross section.

Besides the neutron transfers channels, we also considered the influence of the one-proton (^{10}C,^{9}B) transfer reaction on the elastic scattering. For this particular channel, we consider a model space with the $1f_{7/2}$, $2p_{3/2}$, $1f_{5/2}$, $2p_{1/2}$ and $1g_{9/2}$ orbitals for the valence proton in the target and the *psd* model space for the valence proton in the projectile. The spectroscopic amplitude for both, projectile and target, overlaps were set equal to 1.0. The results of these calculations can also be seen in Fig. 8, given by the green dotted-dashed line. As one can observe this channel has also a very small influence on the elastic scattering cross section. Since there is still room for improvement in the agreement between the calculations and data, breakup reactions were also considered as described in the next section.

V. CONTINUUM DISCRETIZED COUPLED CHANNEL (CDCC)

In the previous section we have considered CC and CRC calculations for elastic scattering in the ^{10}C+^{58}Ni system. Although these calculations were shown to be relevant, they could not fully describe the elastic angular distribution data. The other channel which could be investigated is the breakup, by performing a continuum discretized coupled channel (CDCC) calculation. Since the ^{10}C projectile is a brunnian nucleus, which can break into 2α and $2p$, CDCC calculations need to be performed in a five-body framework. Although four-body calculations have been performed for the ^{6}He(^{4}He+n+n)+^{58}Ni [8] and ^{9}Be(α+α+n)+^{208}Pb [40] systems, five-body CDCC calculations are challenging for theoreticians.

Here, to check the importance of the breakup channels for the ^{10}C+^{58}Ni system, we simplified the configuration of the ^{10}C projectile by assuming that it can be described by ^{9}B+p or ^{6}Be+α cluster configuration. In this case, although ^{9}B and ^{6}Be are unbound and can decay to ^{9}B $\rightarrow$ α+α+p and ^{6}Be $\rightarrow$ α+p+p, we will assume they will remain as a whole system during the breakup. The idea is to check the importance of both breakup channels. Assuming this configuration, we performed three-body, continuum discretized coupled channels (CDCC) calculations. The details about CDCC methods can be found in Refs. [41–44]. Thus, we present only a short description here. A typical coordinate system used in the three-body CDCC for the ^{10}C+^{58}Ni system is shown in Fig. 9, considering the ^{9}B+p configuration.

The CDCC methods solves the Schrödinger equation $(H - E)\mathit{\Psi}(\mathbf{r},\mathbf{R}) = \mathit{0}$, where the wave function with total angular momentum J and z-projection M is written as:

$$\Psi^{JM}(\mathbf{r},\mathbf{R}) = \sum_{\alpha} \frac{F_{\alpha,J}(R)}{R} Y_{\alpha}^{JM}(\mathbf{r},\hat{\mathbf{R}}). \tag{1}$$

Multiplying the Schrödinger equation on the left by the conjugate projectile wave function and using the eq. 1, one obtains the coupled channel equations

$$[T_L + V_{\alpha,\alpha} - (E - \varepsilon_{\alpha})]F_{\alpha,J}(R) + \sum_{\alpha' \neq \alpha} V_{\alpha,\alpha'}(R)F_{\alpha,J}(R) = 0, \tag{2}$$

where T_L is the kinetic energy of relative motion between the projectile and the target; ε_{α} is the intrinsic energy in this channel ($\varepsilon_{\alpha} = e_{\alpha} + \epsilon_{\alpha}$) in which ϵ_{α} is the excitation energy in the corresponding bin state and e_{α} stands for the target's excitation energy. $V_{\alpha,\alpha}$ is the diagonal potential that corresponds to the optical potentials and $V_{\alpha,\alpha'}$ is the potential that couples different states including, the continuum states. The index $\alpha = 0$ denotes the elastic channel, and $\alpha > 0$ represents the excited state of the target or the continuum bins. The matrix elements $V_{\alpha,\alpha'}$ can be write as:

$$V_{\alpha,\alpha'} = \langle \phi_{\alpha}(\mathbf{r}) | V(\mathbf{r},\mathbf{R}) | \phi_{\alpha'}(\mathbf{r}) \rangle \,, \tag{3}$$

where the projectile-target interaction is given by the sum of the proton-target and ^{9}B-target interactions

$$V(\mathbf{r},\mathbf{R}) = V_{p-T}(\mathbf{r_v}) + V_{^9B-T}(\mathbf{r_c}). \tag{4}$$

We also write the projectile-target interaction as

$$V(\mathbf{r},\mathbf{R}) = V_{00}(\mathbf{r},\mathbf{R}) + V_{eff}(\mathbf{r},\mathbf{R}), \tag{5}$$

where V_{00} is the diagonal matrix elements in the elastic channel and V_{eff} is the effective off-diagonal matrix element that takes into account the continuum couplings.

The projectile-target relative-motion wave functions were computed considering partial waves up to L$_{max}$ = 1000$\hbar$ and radii up to R_{coupl}= 500 fm. The discretized bin states were built considering that they are equally spaced in momentum, with maximum energy of ϵ_{bin} = 8 MeV, and with r$_{bin}$ = 60 fm. The potential multipoles were considered up to $\lambda \leq 2$. The complex optical potential, necessary to describe the ^{9}B+^{58}Ni and p-^{58}Ni systems, ^{6}Be+^{58}Ni and α-^{58}Ni systems, were taken as Akyüz-Winther potential, for both real and imaginary parts [45, 46]. This potential has has been very often used in heavy ion scattering analysis. The imaginary part is important to account for the fusion of the fragments with the target. Here we assumed that the imaginary part should have the same form as the real part of the potential, but with a slightly lower depth (multiplied by a factor of 0.78). This procedure has often been used in association with the São Paulo Potential [31, 47], which is similar to the Akyüz-Winther potential at near-barrier energies.

The result of the CDCC calculation as described above is presented in Fig. 10. The previous no-coupling and CC calculations are also ploted for comparison. The CDCC with Akyüz-Winther is not very different from the results of the one-channel CDCC for the ^{10}C(^{9}B+p) configuration, where the latter corresponds to a calculation where all couplings are switched off. This means that coupling to the continuum is not very relevant. Again we should emphasize that this is a simplified CDCC calculation, with a three-body configuration for ^{10}C. Some effect can be observed if we compare the results of the one-channel CDCC with the no-coupling case, which does not take into account the cluster structure of the projectile. By comparing the CDCC one-channel case with the previous results for CC, we see that the agreement with the data is improved by this naive consideration of clusterization in the projectile. This is an indication that the cluster folding potential V_{00}, where we considered explicitly the ^{9}B+^{58}Ni and p-^{58}Ni potentials, might be important. Thus, another possibility was to consider the cluster folding potential, V_{00}, in association with the coupled channel calculation. The V_{00} potential was then used as the real part of the interaction potential , while the imaginary part would be given by the short-range Woods-Saxon potential with the same parameters as used in section III. The results of this calculation, for the ^{9}B+p configuration, is given by the red dotted-dashed solid line in Fig. 10. This result gives a quite good description of the cross sections at backward angles. We also considered the ^{6}Be+α configuration for ^{10}C. However, since this configuration has a higher breakup energy ($S_\alpha = 5.101$ MeV) compared to the breakup energy for the ^{9}B+p channel ($S_p = 4.006$ MeV) and also a higher charge, it is found to be less important. We should mention that this is a simplified model for the ^{10}C configuration and a more realistic calculation would take into account the more realistic $^{10}\mathrm{C} \rightarrow p + p + \alpha + \alpha$ configuration. As mentioned before, this would correspond to a five-body interaction which is still quite a challenge for theorists.

VI. SUMMARY AND CONCLUSIONS

A full angular distribution for the elastic scattering of ^{10}C on ^{58}Ni has been measured at an energy close to the barrier. The obtained angular distributions have been analyzed in terms of coupled channels calculations, where the 2^+ inelastic transition in the projectile has been shown to be of crucial importance to describe the data. The spin reorientation of the 2^+ state in ^{10}C is also important in the elastic process. To improve the agreement with the data we also considered coupled reaction channel calculations with one-neutron, two-neutron and one-proton transfer in the coupling matrix. These transfer reactions were shown to be irrelevant in describing the elastic data. To improve the description of the data we also performed a continuum discretized coupled channel calculations with a simplified cluster configuration for ^{10}C, where the decay channels $^{10}\mathrm{C} \rightarrow {}^{9}\mathrm{B}+p$ and $^{10}\mathrm{C} \rightarrow {}^{6}\mathrm{Be}+\alpha$ were considered. All CC, CRC and CDCC calculations performed here can be considered parameter-free since no parameters were varied.

Our study shows that although the coupling to the continuum itself was not important in the description of the cross sections at backward angles, the cluster folding potential seems to be of importance. We then incorporate the cluster folding model in the CC calculations by using the cluster potential for the $^{9}\mathrm{B}+{}^{58}\mathrm{Ni}$ and $p+{}^{58}\mathrm{Ni}$ fragment systems. The results were very promising and a more realistic calculation should be performed.

We can conclude by saying that our study shows that elastic scattering data can be very useful to understand the key role of target-projectile effects on the nuclear reaction mechanism at energies in the vicinity of the Coulomb barrier. It would be interesting to have a measurement of fusion cross sections for this system for a more complete comparison between fusion, breakup and elastic data.

VII. ACKNOWLEDGMENTS

The author V. G. would like to thank São Paulo Research Foundation (FAPESP) (Grants 2016/02863-4 and 2016/17612-7) and the Conselho Nacional de Desenvolvimento Científico (CNPq) (Grant 304961/2017-5) for the financial support. The authors also thank Brazil INCT-FNA (Instituto Nacional de Ciência e Tecnologia- Física Nuclear e Aplicações), the USA NSF (Grants PHY14-01343 and PHY17-13857) and México CONACYT (Grant CB-

01-254619).

[1] N. Keeley, N. Alamanos, K. W. Kemper, and K. Rusek, Prog. Part. Nucl. Phys. 63, 396 (2009).

[2] L. F. Canto, P. R. S. Gomes, R. Donangelo, J. Lubian, and M. S. Hussein, Phys. Rep. **596**, 1 (2015).

[3] J. J. Kolata, V. Guimarães, E. F. Aguilera, Eur. Phys. J. A **52**, 123 (2016).

[4] I. Tanihata, H. Savajols, R. Kanungo, Prog. Part. Nucl. Phys. **68**, 215 (2013).

[5] P. N. de Faria, R. Lichtenthaler, K. C. C. Pires, A. M. Moro, A. Lepine-Szily, V. Guimaraes, D. R. J. Mendes, A. Arazi, M. Rodrigues-Gallardo, A. Barioni, V.Morcelle, M. C. Morais, O. Camargo, J. Alcantara Nunez and M. Assuncao, Phys Rev. C **81**, 044605 (2010).

[6] L. Acosta, A. M. Sanchez-Benitez, M. E. Gómez, I. Martel, F. Pérez-Bernal, F. Pizarro, J. Rodríguez-Quintero, K. Rusek, M. A. G. Alvarez, M. V. Andrés, *et al.,* Phys. Rev. C **84**, 044604 (2011).

[7] A. M. Sánchez-Beníitez, D. Escrig, M. A. G. Alvarez, M. V. Andrés, C. Angulo, M. J. G. Borge, J. Cabrera, S. Cherubini, P. Demaret, J. M. Espino, *et al.*, Nucl. Phys. A **803**, 30 (2008).

[8] V. Morcelle, K. C. C. Pires, M. Rodriguez-Gallardo, R. Lichtenthaler, A. Lepine-Szily, V. Guimarães, P. N. de Faria, D. R. Mendes, A. M. Moro, L. R. Gasques, *et al.,* Phys. Letter B **732**, 228 (2014).

[9] V. Guimarães, J. J. Kolata, E. F. Aguilera, A. Howard, A. Roberts, F. D. Becchetti, R. O. Torres-Isea, A. Riggins, M. Febrarro, V. Scarduelli, *et al.*, Phys. Rev. C **93**, 064607 (2016).

[10] E. F. Aguilera, J. J. Kolata, F. D. Becchetti, P. A. De Young, J. D Hinnefeld, Á. Horváth, L. O. Lamm, Hye-Young Lee, D. Lizcano, E. Martinez-Quiroz, P. Mohr, T. W. O‘Donnell, D. A. Roberts and G. Rogachev, Phys. Rev. C **63**, 061603(R) (2001).

[11] M. Cubero, J. P. Fernández-García, M. Rodríguez-Gallardo, L. Acosta, M. Acorta, M. A. G. Alvarez, M. J. G. Borge, L. Buchmann, C. A. Diget, H. A. Falou, *et al.*, Phys. Rev. Lett. **109**, 262701 (2012).

[12] N. Keeley, K. W. Kemper, K. Rusek, Phys. Rev. C **88**, 017602 (2013).

[13] A. Di Pietro, V. Scuderi, A. M. Moro, L. Acosta, F. Amorini, M. J. G. Borge, P. Figuera, M. Fisichella, L. M. Fraile, J. Gomez-Camacho, *et al.*, Phys. Rev. C **85**, 054607 (2012).

[14] A. Di Pietro, G. Randisi, V. Scuderi, L. Acosta, F. Amorini, M. J. G, Borge, P. Figuera, M. Fisichella, L. M. Fraile, J. Gomez-Camacho, *et al.*, Phys. Rev. Lett. **105**, 022701 (2010).

[15] N. Keeley, N. Alamanos, K. W. Kemper, K. Rusek, Phys. Rev. C **82**, 034606 (2010).

[16] N. Keeley, K. W. Kemper, K. Rusek, Eur. Phys. J. A **50**, 145 (2014).

[17] E. F. Aguilera, P. Amador-Valenzuela, E. Martinez-Quiroz, J. Fernandez-Arnaiz, J. J. Kolata, V. Guimaraes, Phys Rev. C **93**, 034613 (2016).

[18] E. F. Aguilera, P. Amador-Valenzuela, E. Martinez-Quiroz, D. Lizcano, P. Rosales, H. Garcia-Martinez, A. Gomez-Camacho, J. J. Kolata, A. Roberts, L. O. Lamm, *et al.*, Phys. Rev. Lett. **107**, 092701 (2011).

[19] E. F. Aguilera, E. Martinez-Quiroz, D. Lizcano, A. Gómez-Camacho, J. J. Kolata, L. O. Lamm, V. Guimarães, R. Lichtenthaler, O. Camargo, F. D. Becchetti, *et al.*, Phys. Rev. C **79**, 021601(R) (2009).

[20] J. Lubian, T. Correa, E. F. Aguilera, L. F. Canto, A. Gomez-Camacho, E. M. Quiroz, P. R. S. Gomes Phys. Rev. C **79**, 064605 (2009).

[21] J. Lubian, T. Correa, P. R. S. Gomes, L. F. Canto, Phys. Rev. C **78**, 064615 (2008).

[22] Y. Y. Yang, J. S. Wang, Q. Wang, D. Y. Pang, J. B. Ma, M. R. Huang, J. L. Han, P. Ma, S. L. Jin, Z. Bai, *et al.*, Phys. Rev. C **87**, 044613 (2013).

[23] J. Rangel, J. Lubian, L. F. Canto, P. R. S. Gomes, Phys. Rev. C **93**, 054610 (2016).

[24] Y. Y. Yang, J. S. Wang, Q. Wang, D. Y. Pang, J. B. Ma, M. R. Huang, P. Ma, S. L. Jin, J. L. Han, Z. Bai, *et al.*, Phys. Rev. C **90**, 014606 (2014).

[25] E. F. Aguilera, J J Kolata, E. Martinez-Quiroz, D. Lizcano, P. Amador-Valenzuela, A. Garcia-Flores, D. W. Bardayan, P. D. O'Malley, D. S. Monteiro and V. Morcelle, Journal of Phys.: Conference Series **876**, 012001 (2017).

[26] https://knotplot.com/brunnian/

[27] N. Curtis, N. L. Achouri, N. I. Ashwood, H. G. Bohlen, W. N. Carford, N. M. Clarke, M. Freer, P. J. Haigh, B. Laurent, N. A. Orr, N. P. Patterson, N. Soic, J. S. Thomas and V. Ziman, Phys. Rev. C **77**, 021301(R) (2008).

[28] F. D. Becchetti and J. J. Kolata, Nucl. Instrum. Meth. B **376**, 397 (2016)

[29] F. D. Becchetti, M. Y. Lee, T. W. O'Donnell, D. A. Roberts, J. J. Kolata, L. O. Lamm, G. Rogachev, V. Guimarães, P. A. DeYoung and S. Vicent. Nucl. Instrum. Meth. A **505**, 377 (2003)

[30] I. J. Thompson, Comp. Phys. Rep. 7, 167 (1988).

[31] L. C. Chamon, B. V. Carlson, L. R. Gasques, D. Pereira, C. De Conti, M. A. G. Alvarez, M. S. Hussein, M. A. Candido Ribeiro, E. S. Rossi and C. P. Silva, Phys. Rev. C **66**, 014610 (2002).

[32] E. O. N. Zevallos, V. Guimarães, E. N. Cardozo, J. Lubian, R. Linares, R. Lichtenthaler Filho, K. C. C. Pires, O. C. B. Santos, S. Appannababu, E. Crema, J Alcantara-Nunez, A. L. Lara, Y. S. Villamizar, U. Umbelino, N. Added, M. Assuncao, V. Morcelle, D. S. Monteiro, Phys. Rev. C **99**, 064613 (2019).

[33] V. Scarduelli, E. Crema, V. Guimarães, D. Abriola, A. Arazi, E. de Barbará, O. A. Capurro, M. A. Cardonna, J. Gallardo, D. Hojman, G. V. Marti, A. J. Pacheco, D. Rodrigues, Y. Y. Yang, N. N. Deshmukh, B. Paes, J. Lubian, D. R. Mendes Jr, V. Morcelle and D. S. Monteiro, Phys. Rev. C, 96, 054610 (2017).

[34] N. N. Deshmukh, V. Guimarães, E. Crema, D. Abriola, A. Arazi, E. de Barbará, O. A. Capurro, M. A. Cardona, J. Gallardo, D. Hojman, G. V. Marti, A. J. Pacheco, D. Rodrigues, Y. Y. Yang, A. N. Deshmukh, D. R. Mendes, V. Morcelle, V. Scarduelli and D. S. Monteiro, Phys. Rev. C **92**, 054615 (2015).

[35] Evaluated Nuclear Structure Data Files, National Nuclear Data Center, Brookhaven National Laboratory [http://www.nndc.bnl.gov].

[36] S. Raman, C. W. Nestor, P. Tikkanen, Atomic Data and Nuclear Data Tables **78**, 1 (2001).

[37] W. D. M. Rae, http://www.garsington.eclipse.co.uk (2008).

[38] Y. Utsuno and S. Chiba, Phys. Rev. C **83**, 021301(R) (2011).

[39] L. Coraggio, A. Covello, A. Gargano and N. Itaco, Phys. Rev. C **89**, 024319 (2014).

[40] P. Descouvemont, T. Druet, L. F. Canto, M. S. Hussein, Phys. Rev. C **91**, 024606 (2015).

[41] M. Kamimura, M. Yahiro and Y. Iseri, Prog. Theor. Phys. Suppl. **89**,1(1986).

[42] N. Austern, Y. Iseri, M. Kamamura, M. Kawai, G. Rawitscher and M. Yashiro, Phys. Rep. **154**, 125 (1987).

[43] M. Y. Ahiro, M. Nakano,Y. Iseri and M. Kamimura, Prog. Theor. Phys. **67**, 5 (1982)

[44] P. Descouvemont, L. F. Canto and M. S. Hussein. Phys. Rev. C **95**, 014604 (2017).

[45] R. A. Broglia and A. Winther, Heavy Ion Reactions, Westview Press, Boulder, CO (2004).

[46] R. O. Akyüz and A. Winther. 1981. Proc. Enrico Fermi Int. School of Physics, 1979, Nuclear structure and heavy-ion reactions, R. A. Broglia, C. H. Dasso and R. Ricci (eds.) (NorthHol-

land, Amsterdam), p. 491.

[47] L. R. Gasques, L. C. Chamon, P. R. S. Gomes, and J. Lubian, Nucl. Phys. A **764** ,135 (2006).

TABLE I: Spin-parity and energy of the states in ^{58}Ni and ^{10}C, from the NNDC database [35], considered in the coupled-channel calculations.

^{58}Ni		^{10}C	
J^π	E (MeV)	J^π	E (MeV)
0^+	g.s.	0^+	g.s.
2^+	1.454	2^+	3.354
4^+	2.459		
2^+	2.775		
0^+	2.942		
3^-	4.475		

TABLE II: The *E2* inelastic transitions for ^{10}C used in the coupled-channel calculations.

E (keV)	E_γ (keV)	$J_F \rightarrow J_i$	$B(E2)$ (W.u.)	$< J_f\|E2\|J_i >$ (e^2fm^4)	δ_2 (fm)
3353.7	3353.6	$2^+ \rightarrow 0^+$	9.5 (15)	7.947	2.429

TABLE III: All *E2* inelastic transitions for ^{58}Ni used in the coupled-channel calculations.

E (keV)	E_γ (keV)	$J_F \rightarrow J_i$	$B(E2)$ (W.u.)	$< J_f\|E2\|J_i >$ (e^2fm^4)	δ_2 (fm)
1454.28	1454.28	$0^+ \rightarrow 2^+$	10 (4)	26.365	0.941
2459.21	1004.8	$2^+ \rightarrow 4^+$	11.2 (12)	80.189	2.923
2775.42	1321.2	$2^+ \rightarrow 2^+$	15 (4)	-44.523	-1.623
2942.56	1488.3	$2^+ \rightarrow 0^+$	21 (3)	16.667	0.608

TABLE IV: The *E3* inelastic transition for ^{58}Ni used in the coupled-channel calculations.

E (keV)	E_γ (keV)	$J_F \rightarrow J_i$	$B(E3)$ (e^2 b^3)	$< J_f \vert E3 \vert J_i >$ ($e^2 fm^4$)	δ_3 (fm)
4474.6	4474.6	$0^+ \rightarrow 3^-$	0.0195 (27)	112.443	0.9991

TABLE V: Reorientation parameters used in the coupled channel calculations.

Nucleus	E_{level} (MeV)	J^π	Q_2 (fm^2)	$< J_f \vert M(E2) \vert J_i >$ (e^{2}fm^4)	δ_2 (fm)	β_2
^{10}C	3.3537	2^+		-9.498	-2.903	0.83 (7)
^{58}Ni	1.4542	2^+	-10 (6)	13.1938	0.481	0.098

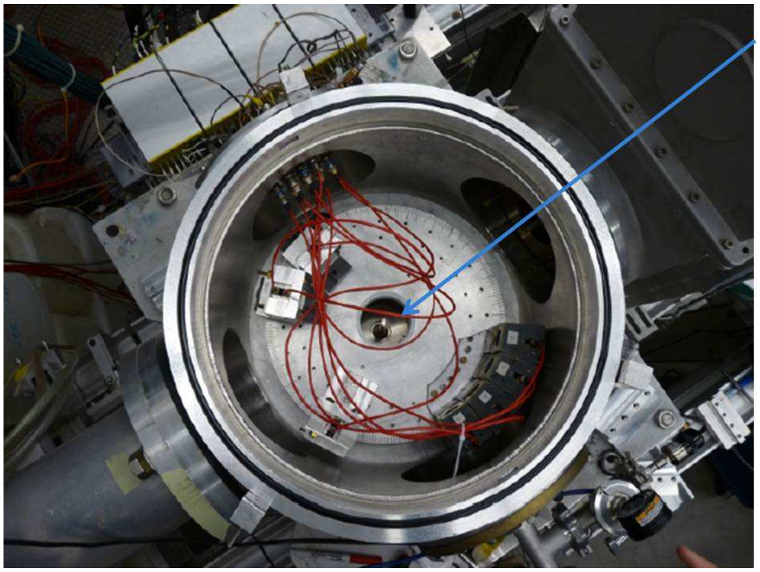

FIG. 1: A picture of the detection setup. The beam direction is indicated.

TABLE VI: Spectroscopic amplitudes used in the CRC calculations for one-neutron transfer using the *psdpn* model space with the *psdmod* effective phenomenological interaction for the projectile overlap and *bjuff* model space with the effective phenomenological *48Cauff* interaction for the target overlap.

Initial state	Final state	*nlj*	Spect. ampl.
$^{10}\mathrm{C}_{g.s}(0^{+})$	$^{11}\mathrm{C}_{g.s}(3/2^{-})$	$1p_{3/2}$	-0.654
$^{10}\mathrm{C}_{g.s}(0^{+})$	$^{11}\mathrm{C}_{2.000}(1/2^{-})$	$1p_{1/2}$	-0.647
$^{10}\mathrm{C}_{g.s}(0^{+})$	$^{11}\mathrm{C}_{4.804}(3/2^{-})$	$1p_{3/2}$	-0.112
$^{10}\mathrm{C}_{3.354}(2^{+})$	$^{11}\mathrm{C}_{g.s}(3/2^{-})$	$1p_{1/2}$	0.080
		$1p_{3/2}$	1.282
$^{10}\mathrm{C}_{3.354}(2^{+})$	$^{11}\mathrm{C}_{2.000}(1/2^{-})$	$1p_{3/2}$	0.280
$^{10}\mathrm{C}_{3.354}(2^{+})$	$^{11}\mathrm{C}_{4.318}(5/2^{-})$	$1p_{1/2}$	0.665
		$1p_{3/2}$	-0.537
$^{10}\mathrm{C}_{3.354}(2^{+})$	$^{11}\mathrm{C}_{4.804}(3/2^{-})$	$1p_{1/2}$	-0.614
		$1p_{3/2}$	-0.123
$^{58}\mathrm{Ni}_{g.s}(0^{+})$	$^{57}\mathrm{Ni}_{g.s}(3/2^{-})$	$2p_{3/2}$	-1.041
$^{58}\mathrm{Ni}_{g.s}(0^{+})$	$^{57}\mathrm{Ni}_{0.768}(5/2^{-})$	$1f_{5/2}$	-0.752
$^{58}\mathrm{Ni}_{g.s}(0^{+})$	$^{57}\mathrm{Ni}_{1.113}(1/2^{-})$	$2p_{1/2}$	-0.520
$^{58}\mathrm{Ni}_{g.s}(0^{+})$	$^{57}\mathrm{Ni}_{2.443}(5/2^{-})$	$1f_{5/2}$	-0.054
$^{58}\mathrm{Ni}_{g.s}(0^{+})$	$^{57}\mathrm{Ni}_{3.007}(3/2^{-})$	$2p_{3/2}$	-0.084
$^{58}\mathrm{Ni}_{1.454}(2^{+})$	$^{57}\mathrm{Ni}_{g.s}(3/2^{-})$	$2p_{1/2}$	0.487
		$2p_{3/2}$	0.784
		$1f_{5/2}$	0.300
$^{58}\mathrm{Ni}_{1.454}(2^{+})$	$^{57}\mathrm{Ni}_{0.768}(5/2^{-})$	$2p_{1/2}$	0.394
		$2p_{3/2}$	-0.306
		$1f_{5/2}$	0.416
$^{58}\mathrm{Ni}_{1.454}(2^{+})$	$^{57}\mathrm{Ni}_{1.113}(1/2^{-})$	$2p_{3/2}$	-0.507
		$1f_{5/2}$	0.396
$^{58}\mathrm{Ni}_{1.454}(2^{+})$	$^{57}\mathrm{Ni}_{2.443}(5/2^{-})$	$2p_{1/2}$	0.055
		$2p_{3/2}$	-0.073
		$1f_{5/2}$	-0.024

TABLE VII: Table VI continued

.

Initial state	Final state	*nlj*	Spect. ampl.
$^{58}\mathrm{Ni}_{1.454}(2^{+})$	$^{57}\mathrm{Ni}_{2.557}(7/2^{-})$	$2p_{3/2}$	-0.103
		$1f_{5/2}$	-0.057
$^{58}\mathrm{Ni}_{1.454}(2^{+})$	$^{57}\mathrm{Ni}_{3.007}(3/2^{-})$	$2p_{1/2}$	0.043
		$2p_{3/2}$	-0.033
		$1f_{5/2}$	0.065
$^{58}\mathrm{Ni}_{1.454}(2^{+})$	$^{57}\mathrm{Ni}_{3.230}(7/2^{-})$	$2p_{3/2}$	0.228
		$1f_{5/2}$	-0.0001
$^{58}\mathrm{Ni}_{2.459}(4^{+})$	$^{57}\mathrm{Ni}_{g.s}(3/2^{-})$	$1f_{5/2}$	0.867
$^{58}\mathrm{Ni}_{2.459}(4^{+})$	$^{57}\mathrm{Ni}_{0.768}(5/2^{-})$	$2p_{3/2}$	-0.901
		$1f_{5/2}$	0.383
$^{58}\mathrm{Ni}_{2.459}(4^{+})$	$^{57}\mathrm{Ni}_{2.443}(5/2^{-})$	$2p_{3/2}$	0.458
		$1f_{5/2}$	0.160
$^{58}\mathrm{Ni}_{2.459}(4^{+})$	$^{57}\mathrm{Ni}_{2.557}(7/2^{-})$	$2p_{1/2}$	-0.066
		$2p_{3/2}$	-0.019
		$1f_{5/2}$	-0.116
$^{58}\mathrm{Ni}_{2.459}(4^{+})$	$^{57}\mathrm{Ni}_{3.007}(3/2^{-})$	$2p_{3/2}$	0.043
		$1f_{5/2}$	-0.033
$^{58}\mathrm{Ni}_{2.459}(4^{+})$	$^{57}\mathrm{Ni}_{3.230}(7/2^{-})$	$2p_{1/2}$	0.175
		$2p_{3/2}$	0.063
		$1f_{5/2}$	0.185

TABLE VIII: Table VII continued.

Initial state	Final state	nlj	Spect. ampl.
$^{58}\mathrm{Ni}_{2.775}(2^+)$	$^{57}\mathrm{Ni}_{g.s}(3/2^-)$	$2p_{1/2}$	-0.403
		$2p_{3/2}$	0.890
		$1f_{5/2}$	0.027
$^{58}\mathrm{Ni}_{2.775}(2^+)$	$^{57}\mathrm{Ni}_{0.768}(5/2^-)$	$2p_{1/2}$	-0.236
		$2p_{3/2}$	-0.044
		$1f_{5/2}$	-0.468
$^{58}\mathrm{Ni}_{2.775}(2^+)$	$^{57}\mathrm{Ni}_{1.113}(1/2^-)$	$2p_{3/2}$	0.426
		$1f_{5/2}$	-0.244
$^{58}\mathrm{Ni}_{2.775}(2^+)$	$^{57}\mathrm{Ni}_{2.443}(5/2^-)$	$2p_{1/2}$	0.153
		$2p_{3/2}$	-0.521
		$1f_{5/2}$	-0.078
$^{58}\mathrm{Ni}_{2.775}(2^+)$	$^{57}\mathrm{Ni}_{2.557}(7/2^-)$	$2p_{3/2}$	-0.042
		$1f_{5/2}$	0.0001
$^{58}\mathrm{Ni}_{2.775}(2^+)$	$^{57}\mathrm{Ni}_{3.007}(3/2^-)$	$2p_{1/2}$	-0.057
		$2p_{3/2}$	0.013
		$1f_{5/2}$	0.069
$^{58}\mathrm{Ni}_{2.775}(2^+)$	$^{57}\mathrm{Ni}_{3.230}(7/2^-)$	$2p_{3/2}$	0.158
		$1f_{5/2}$	-0.214
$^{58}\mathrm{Ni}_{2.942}(0^+)$	$^{57}\mathrm{Ni}_{g.s}(3/2^-)$	$2p_{3/2}$	0.776
$^{58}\mathrm{Ni}_{2.942}(0^+)$	$^{57}\mathrm{Ni}_{0.768}(5/2^-)$	$1f_{5/2}$	-1.044
$^{58}\mathrm{Ni}_{2.942}(0^+)$	$^{57}\mathrm{Ni}_{1.113}(1/2^-)$	$2p_{1/2}$	-0.141
$^{58}\mathrm{Ni}_{2.942}(0^+)$	$^{57}\mathrm{Ni}_{2.443}(5/2^-)$	$1f_{5/2}$	0.208
$^{58}\mathrm{Ni}_{2.942}(0^+)$	$^{57}\mathrm{Ni}_{3.007}(3/2^-)$	$2p_{3/2}$	0.254
$^{58}\mathrm{Ni}_{4.475}(3^-)$	$^{57}\mathrm{Ni}_{g.s}(3/2^-)$	$1g_{9/2}$	0.902
$^{58}\mathrm{Ni}_{4.475}(3^-)$	$^{57}\mathrm{Ni}_{0.768}(5/2^-)$	$1g_{9/2}$	-0.289
$^{58}\mathrm{Ni}_{4.475}(3^-)$	$^{57}\mathrm{Ni}_{2.443}(5/2^-)$	$1g_{9/2}$	-0.219
$^{58}\mathrm{Ni}_{4.475}(3^-)$	$^{57}\mathrm{Ni}_{2.557}(7/2^-)$	$1g_{9/2}$	-0.114
$^{58}\mathrm{Ni}_{4.475}(3^-)$	$^{57}\mathrm{Ni}_{3.007}(3/2^-)$	$1g_{9/2}$	0.132
$^{58}\mathrm{Ni}_{4.475}(3^-)$	$^{57}\mathrm{Ni}_{3.230}(7/2^-)$	$1g_{9/2}$	0.106

TABLE IX: Spectroscopic amplitudes used in the CRC calculations for two-neutron transfer using the *psdpn* model space with the effective phenomenological *psdmod* interaction for the projectile overlap. Here $(n1l1j1)(n2l2j2)$ are the principal quantum numbers, the orbital angular momentum, and the total angular momenta of the neutrons 1 and 2 with espect to the core. *J12* is the angular momentum of the two-neutron system.

Initial state	$(n1l1j1)(n2l2j2)$	Final state	*J12*	Spect. ampl.
$^{10}\mathrm{C}_{g.s}(0^+)$	$(1p_{3/2})^2$	$^{12}\mathrm{C}_{g.s}(0^+)$	0	0.836
	$(1p_{1/2})^2$			0.334
	$(1d_{5/2})^2$			-0.060
	$(1d_{3/2})^2$			-0.040
	$(2s_{1/2})^2$			-0.006
$^{10}\mathrm{C}_{g.s}(0^+)$	$(1p_{3/2})^2$	$^{12}\mathrm{C}_{4.439}(2^+)$	2	-0.028
	$(1p_{3/2})(1p_{1/2})$			0.389
	$(1d_{5/2})^2$			0.050
	$(1d_{5/2})(1d_{3/2})$			-0.016
	$(1d_{5/2})(2s_{1/2})$			-0.005
	$(1d_{3/2})^2$			0.027
	$(1d_{3/2})(2s_{1/2})$			-0.004
$^{10}\mathrm{C}_{g.s}(0^+)$	$(1p_{3/2})^2$	$^{12}\mathrm{C}_{7.654}(0^+)$	0	-0.296
	$(1p_{1/2})^2$			0.250
	$(1d_{5/2})^2$			-0.153
	$(1d_{3/2})^2$			-0.039
	$(2s_{1/2})^2$			-0.035
$^{10}\mathrm{C}_{g.s}(0^+)$	$(1p_{3/2})(1d_{5/2})$	$^{12}\mathrm{C}_{9.641}(3^-)$	3	0.281
	$(1p_{3/2})(1d_{3/2})$			-0.181
	$(1p_{1/2})(1d_{5/2})$			0.174

TABLE X: Table IX continued.

Initial state	$(n1l1j1)(n2l2j2)$	Final state	$J12$	Spect. ampl.
$^{10}\mathrm{C}_{3.354}(2^+)$	$(1p_{3/2})^2$	$^{12}\mathrm{C}_{g.s.}(0^+)$	2	-1.536
	$(1p_{3/2})(1p_{1/2})$			0.201
	$(1d_{5/2})^2$			-0.060
	$(1d_{5/2})(1d_{3/2})$			-0.020
	$(1d_{5/2})(2s_{1/2})$			-0.002
	$(1d_{3/2})^2$			-0.018
	$(1d_{3/2})(2s_{1/2})$			-0.009
$^{10}\mathrm{C}_{3.354}(2^+)$	$(1p_{3/2})^2$	$^{12}\mathrm{C}_{4.439}(2^+)$	0	-0.296
	$(1p_{1/2})^2$			-0.243
	$(1d_{5/2})^2$			0.049
	$(1d_{3/2})^2$			0.009
	$(2s_{1/2})^2$			0.005
$^{10}\mathrm{C}_{3.354}(2^+)$	$(1p_{3/2})^2$	$^{12}\mathrm{C}_{7.654}(0^+)$	2	0.700
	$(1p_{3/2})(1p_{1/2})$			0.168
	$(1d_{5/2})^2$			-0.088
	$(1d_{5/2})(1d_{3/2})$			0.014
	$(1d_{5/2})(2s_{1/2})$			-0.037
	$(1d_{3/2})^2$			-0.018
	$(1d_{3/2})(2s_{1/2})$			0.001
$^{10}\mathrm{C}_{3.354}(2^+)$	$(1p_{3/2})(1d_{5/2})$	$^{12}\mathrm{C}_{9.641}(3^-)$	1	-0.410
	$(1p_{3/2})(1d_{3/2})$			0.142
	$(1p_{3/2})(2s_{1/2})$			-0.001
	$(1p_{1/2})(1d_{3/2})$			-0.197
	$(1p_{1/2})(2s_{1/2})$			-0.001

TABLE XI: Spectroscopic amplitudes used in the CRC calculations for two-neutron transfer using the *bjuff* model space with the effective phenomenological *48Cauff* interaction for the target overlaps.

Initial state	*(n1l1j1)(n2l2j2)*	Final State	*J12*	Spect. ampl.
$^{58}\mathrm{Ni}_{g.s}(0^+)$	$(1f_{5/2})^2$	$^{56}\mathrm{Ni}_{g.s}(0^+)$	0	-0.459
	$(2p_{3/2})^2$			-0.662
	$(2p_{1/2})^2$			-0.301
	$(1g_{9/2})^2$			0.132
$^{58}\mathrm{Ni}_{g.s}(0^+)$	$(1f_{5/2})^2$	$^{56}\mathrm{Ni}_{2.701}(2^+)$	2	-0.170
	$(1f_{5/2})(2p_{3/2})$			-0.170
	$(1f_{5/2})(2p_{1/2})$			-0.193
	$(2p_{3/2})^2$			-0.235
	$(2p_{3/2})(2p_{1/2})$			0.210
	$(1g_{9/2})^2$			0.040
$^{58}\mathrm{Ni}_{g.s}(0^+)$	$(1f_{5/2})^2$	$^{56}\mathrm{Ni}_{3.924}(4^+)$	4	-0.050
	$(1f_{5/2})(2p_{3/2})$			-0.146
	$(1g_{9/2})^2$			0.009
$^{58}\mathrm{Ni}_{g.s}(0^+)$	$(1f_{5/2})^2$	$^{56}\mathrm{Ni}_{3.957}(0^+)$	0	-0.016
	$(2p_{3/2})^2$			-0.053
	$(2p_{1/2})^2$			-0.036
	$(1g_{9/2})^2$			0.007
$^{58}\mathrm{Ni}_{1.454}(2^+)$	$(1f_{5/2})^2$	$^{56}\mathrm{Ni}_{g.s.}(0^+)$	2	-0.258
	$(1f_{5/2})(2p_{3/2})$			-0.263
	$(1f_{5/2})(2p_{1/2})$			-0.324
	$(2p_{3/2})^2$			-0.511
	$(2p_{3/2})(2p_{1/2})$			0.429
	$(1g_{9/2})^2$			0.059
$^{58}\mathrm{Ni}_{1.454}(2^+)$	$(1f_{5/2})^2$	$^{56}\mathrm{Ni}_{2.701}(2^+)$	0	-0.154
	$(2p_{3/2})^2$			-0.255
	$(2p_{1/2})^2$			-0.149
	$(1g_{9/2})^2$			0.046

TABLE XII: Table XI continued.

Initial state	*(n1l1j1)(n2l2j2)*	Final state	*J12*	Spect. ampl.
$^{58}\mathrm{Ni}_{1.454}(2^+)$	$(1f_{5/2})^2$	$^{56}\mathrm{Ni}_{3.924}(4^+)$	2	-0.027
	$(1f_{5/2})(2p_{3/2})$			-0.037
	$(1f_{5/2})(2p_{1/2})$			-0.055
	$(2p_{3/2})^2$			-0.050
	$(2p_{3/2})(2p_{1/2})$			0.049
	$(1g_{9/2})^2$			0.008
$^{58}\mathrm{Ni}_{1.454}(2^+)$	$(1f_{5/2})^2$	$^{56}\mathrm{Ni}_{3.957}(0^+)$	2	-0.008
	$(1f_{5/2})(2p_{3/2})$			-0.015
	$(1f_{5/2})(2p_{1/2})$			-0.026
	$(2p_{3/2})^2$			-0.040
	$(2p_{3/2})(2p_{1/2})$			0.047
	$(1g_{9/2})^2$			0.004
$^{58}\mathrm{Ni}_{2.459}(4^+)$	$(1f_{5/2})^2$	$^{56}\mathrm{Ni}_{g.s}(0^+)$	4	-0.238
	$(1f_{5/2})(2p_{3/2})$			-0.799
	$(1g_{9/2})^2$			0.034
$^{58}\mathrm{Ni}_{2.459}(4^+)$	$(1f_{5/2})^2$	$^{56}\mathrm{Ni}_{2.701}(2^+)$	2	-0.062
	$(1f_{5/2})(2p_{3/2})$			0.087
	$(1f_{5/2})(2p_{1/2})$			-0.142
	$(2p_{3/2})^2$			-0.100
	$(2p_{3/2})(2p_{1/2})$			-0.195
	$(1g_{9/2})^2$			0.018
$^{58}\mathrm{Ni}_{2.459}(4^+)$	$(1f_{5/2})^2$	$^{56}\mathrm{Ni}_{3.924}(4^+)$	0	-0.058
	$(2p_{3/2})^2$			-0.084
	$(2p_{1/2})^2$			-0.033
	$(1g_{9/2})^2$			0.015
$^{58}\mathrm{Ni}_{2.459}(4^+)$	$(1f_{5/2})^2$	$^{56}\mathrm{Ni}_{3.975}(0^+)$	4	-0.005
	$(1f_{5/2})(2p_{3/2})$			0.033
	$(1g_{9/2})^2$			0.001

TABLE XIII: Table XII continued.

Initial state	*(n1l1j1)(n2l2j2)*	Final state	*J12*	Spect. ampl.
$^{58}\mathrm{Ni}_{2.775}(2^+)$	$(1f_{5/2})^2$	$^{56}\mathrm{Ni}_{g.s.}(0^+)$	2	0.296
	$(1f_{5/2})(2p_{3/2})$			-0.020
	$(1f_{5/2})(2p_{1/2})$			0.210
	$(2p_{3/2})^2$			-0.599
	$(2p_{3/2})(2p_{1/2})$			-0.364
	$(1g_{9/2})^2$			0.0005
$^{58}\mathrm{Ni}_{2.775}(2^+)$	$(1f_{5/2})^2$	$^{56}\mathrm{Ni}_{2.701}(2^+)$	0	-0.009
	$(2p_{3/2})^2$			-0.026
	$(2p_{1/2})^2$			-0.022
	$(1g_{9/2})^2$			0.004
$^{58}\mathrm{Ni}_{2.775}(2^+)$	$(1f_{5/2})^2$	$^{56}\mathrm{Ni}_{3.924}(4^+)$	2	0.014
	$(1f_{5/2})(2p_{3/2})$			-0.086
	$(1f_{5/2})(2p_{1/2})$			0.076
	$(2p_{3/2})^2$			-0.007
	$(2p_{3/2})(2p_{1/2})$			-0.015
	$(1g_{9/2})^2$			0.001
$^{58}\mathrm{Ni}_{2.775}(2^+)$	$(1f_{5/2})^2$	$^{56}\mathrm{Ni}_{3.957}(0^+)$	2	0.006
	$(1f_{5/2})(2p_{3/2})$			0.002
	$(1f_{5/2})(2p_{1/2})$			0.013
	$(2p_{3/2})^2$			-0.037
	$(2p_{3/2})(2p_{1/2})$			0.036
	$(1g_{9/2})^2$			0.0003

TABLE XIV: Table XIII continued.

Initial state	$(n1l1j1)(n2l2j2)$	Final state	$J12$	Spect. ampl.
$^{58}\mathrm{Ni}_{2.942}(0^+)$	$(1f_{5/2})^2$	$^{56}\mathrm{Ni}_{g.s}(0^+)$	0	-0.661
	$(2p_{3/2})^2$			0.489
	$(2p_{1/2})^2$			-0.080
	$(1g_{9/2})^2$			0.048
$^{58}\mathrm{Ni}_{2.942}(0^+)$	$(1f_{5/2})^2$	$^{56}\mathrm{Ni}_{2.701}(2^+)$	2	-0.366
	$(1f_{5/2})(2p_{3/2})$			0.091
	$(1f_{5/2})(2p_{1/2})$			-0.163
	$(2p_{3/2})^2$			0.284
	$(2p_{3/2})(2p_{1/2})$			-0.083
	$(1g_{9/2})^2$			0.005
$^{58}\mathrm{Ni}_{2.942}(0^+)$	$(1f_{5/2})^2$	$^{56}\mathrm{Ni}_{3.924}(4^+)$	4	-0.124
	$(1f_{5/2})(2p_{3/2})$			0.017
	$(1g_{9/2})^2$			0.002
$^{58}\mathrm{Ni}_{2.942}(0^+)$	$(1f_{5/2})^2$	$^{56}\mathrm{Ni}_{3.957}(0^+)$	0	0.009
	$(2p_{3/2})^2$			0.082
	$(2p_{1/2})^2$			0.021
	$(1g_{9/2})^2$			-0.008
$^{58}\mathrm{Ni}_{4.475}(3^-)$	$(1f_{5/2})(1g_{9/2})$	$^{56}\mathrm{Ni}_{g.s.}(0^+)$	3	0.248
	$(2p_{3/2})(1g_{9/2})$			0.817
$^{58}\mathrm{Ni}_{4.475}(3^-)$	$(1f_{5/2})(1g_{9/2})$	$^{56}\mathrm{Ni}_{2.701}(2^+)$	3	0.085
	$(2p_{3/2})(1g_{9/2})$			0.330
$^{58}\mathrm{Ni}_{4.475}(3^-)$	$(1f_{5/2})(1g_{9/2})$	$^{56}\mathrm{Ni}_{3.924}(4^+)$	3	0.001
	$(2p_{3/2})(1g_{9/2})$			0.062
$^{58}\mathrm{Ni}_{4.475}(3^-)$	$(1f_{5/2})(1g_{9/2})$	$^{56}\mathrm{Ni}_{3.957}(0^+)$	3	0.817
	$(2p_{3/2})(1g_{9/2})$			-0.257

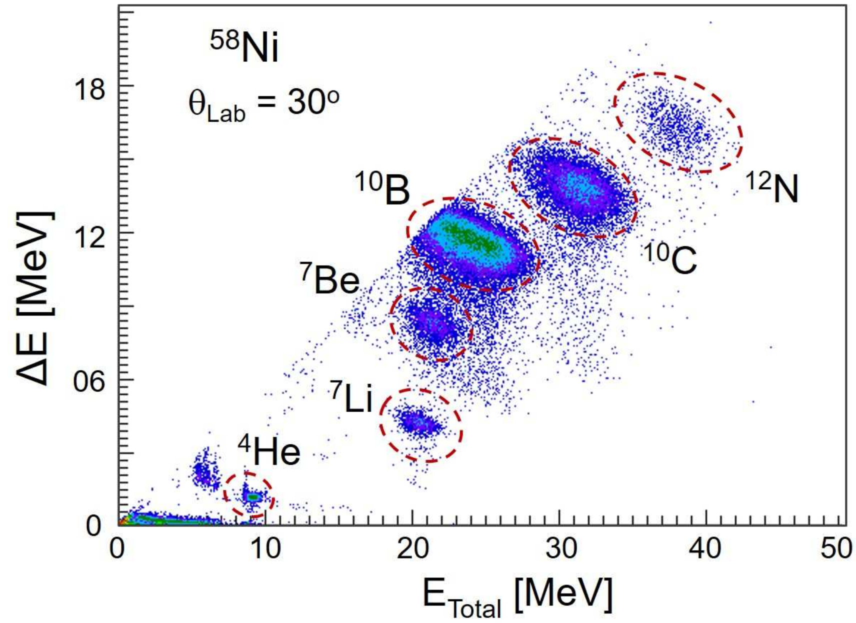

FIG. 2: A typical two-dimensional $\Delta E - E_{\mathrm{Total}}$ spectrum for ^{10}C+^{58}Ni at E_{Lab}= 35.3 MeV and θ_{Lab}= 30.0^0. The contributions of each beam contaminant are indicated.

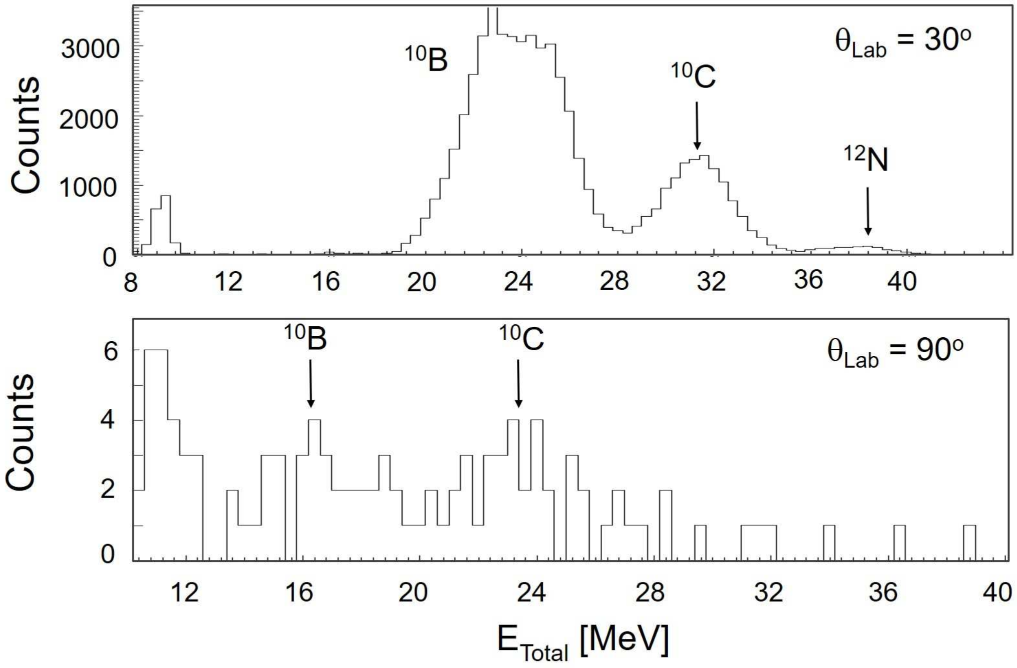

FIG. 3: Energy spectra for ^{10}C+^{58}Ni at (a) θ_{Lab}= 30.0^0 and (b) 90.0^0. The peak for ^{10}C and the one corresponding to the scattered primary beam contaminant ^{10}B are indicated.

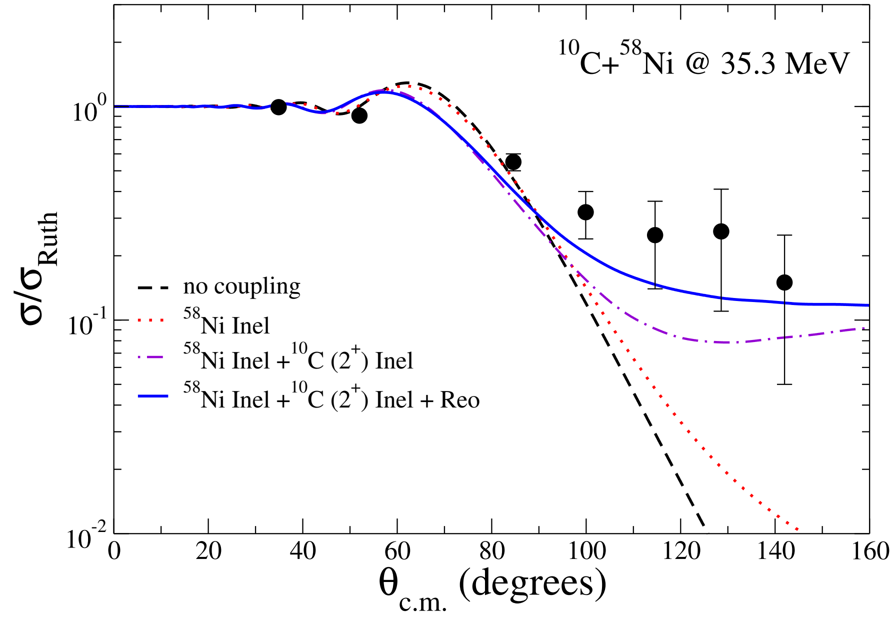

FIG. 4: Elastic scattering angular distribution for the ^{10}C+^{58}Ni system at E_{Lab}=35.3 MeV. The curves are results of coupled-channel calculations as indicated. "Reo" implies inclusion of reorientation effects.

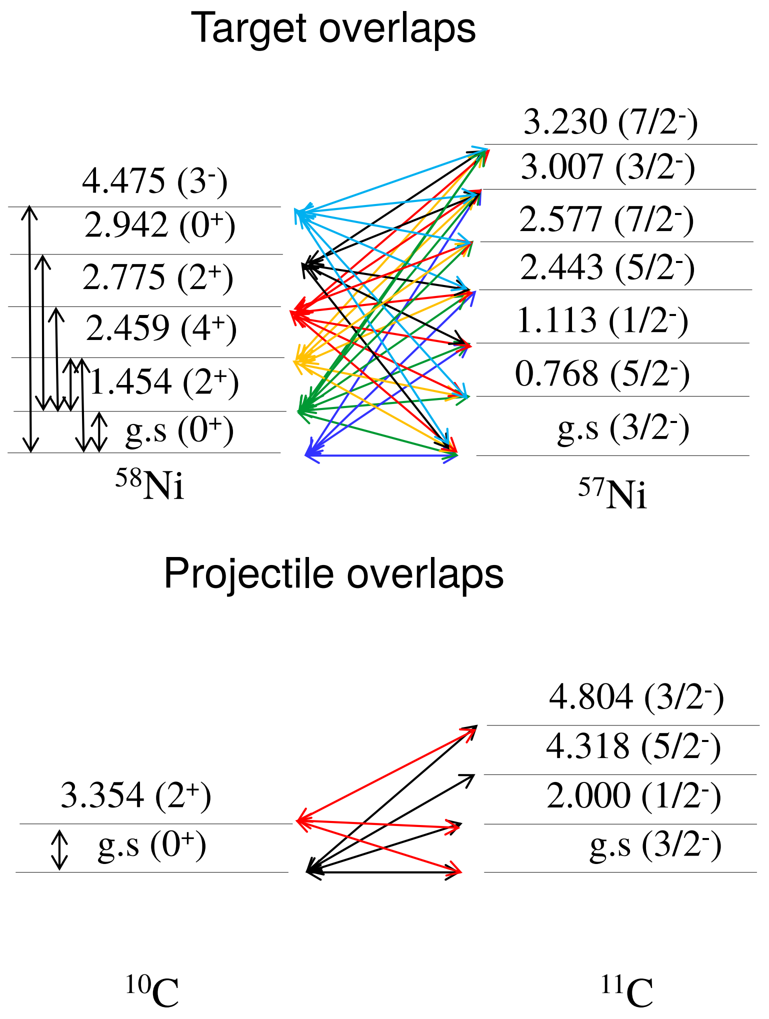

FIG. 5: Coupling scheme of the projectile and target overlaps used in the one-neutron transfer reaction calculation.

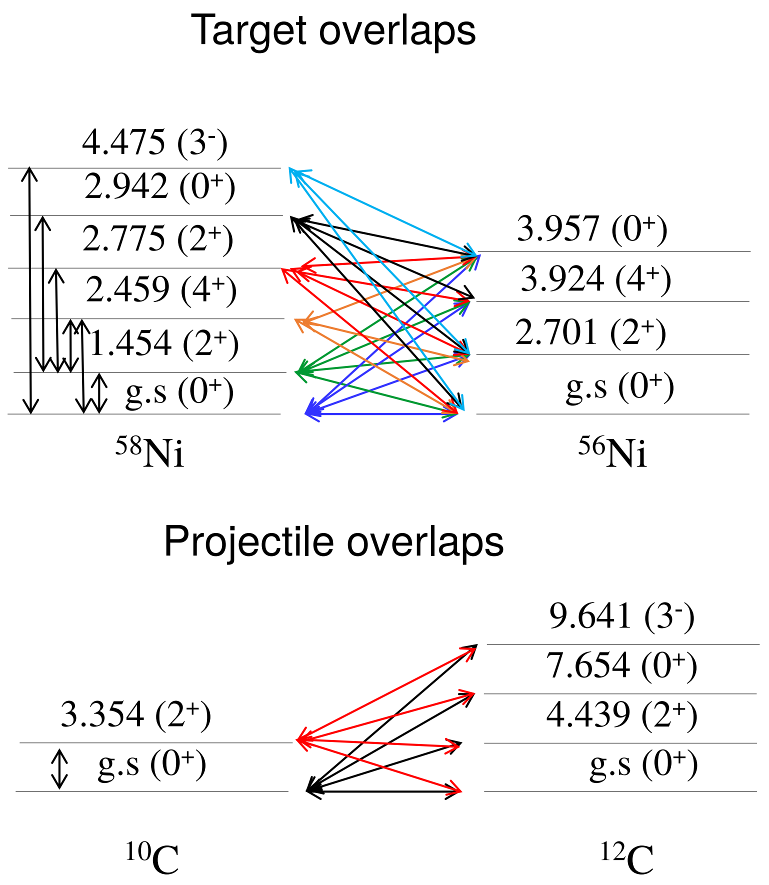

FIG. 6: Coupling scheme of the projectile and target overlaps used in the two-neutron transfer reaction calculations.

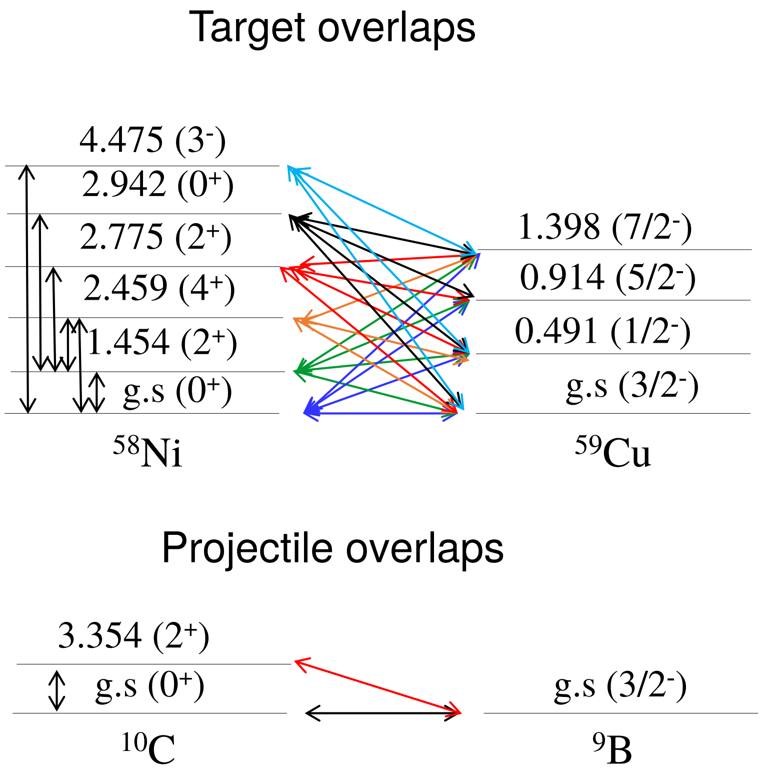

FIG. 7: Coupling scheme of the projectile and target overlaps used in the one-proton transfer reaction calculations.

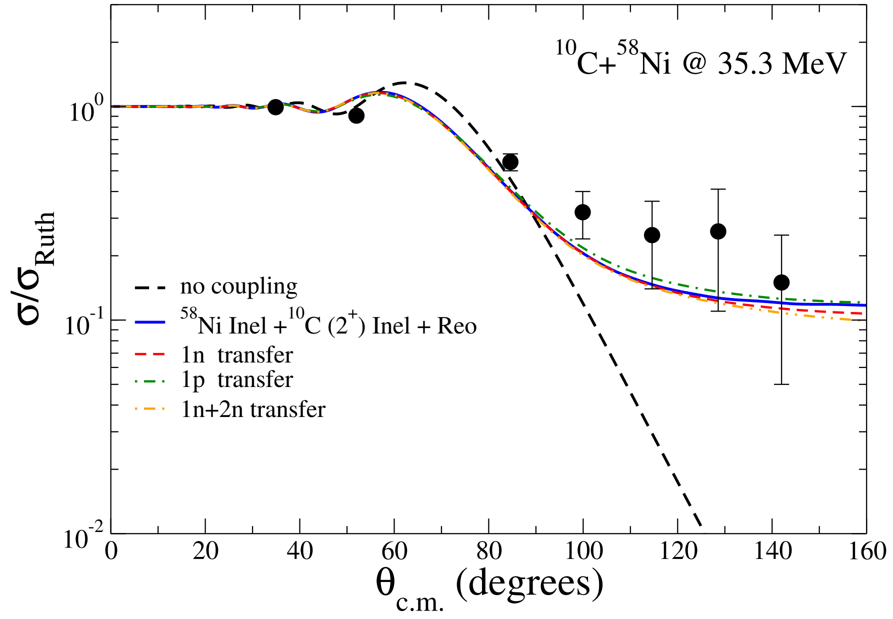

FIG. 8: Elastic scattering angular distributions for the ^{10}C+^{58}Ni system at $E_{\mathrm{Lab}} = 35.3$ MeV. The curves are results of coupled reaction channel calculations as indicated. "Reo" implies inclusion of reorientation effects.

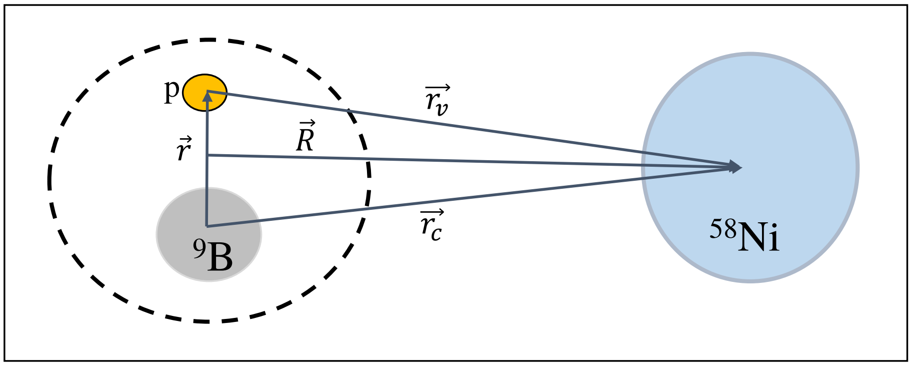

FIG. 9: Coordinate system used in three-body CDCC. $\vec{r}$ is the coordinate that connects the center of the core and the proton; $\vec{r}_v$ and $\vec{r}_c$ are the position vectors of the valence particle and core in relation to the target, respectively. $\vec{R}$ is the projectile-target relative coordinate.

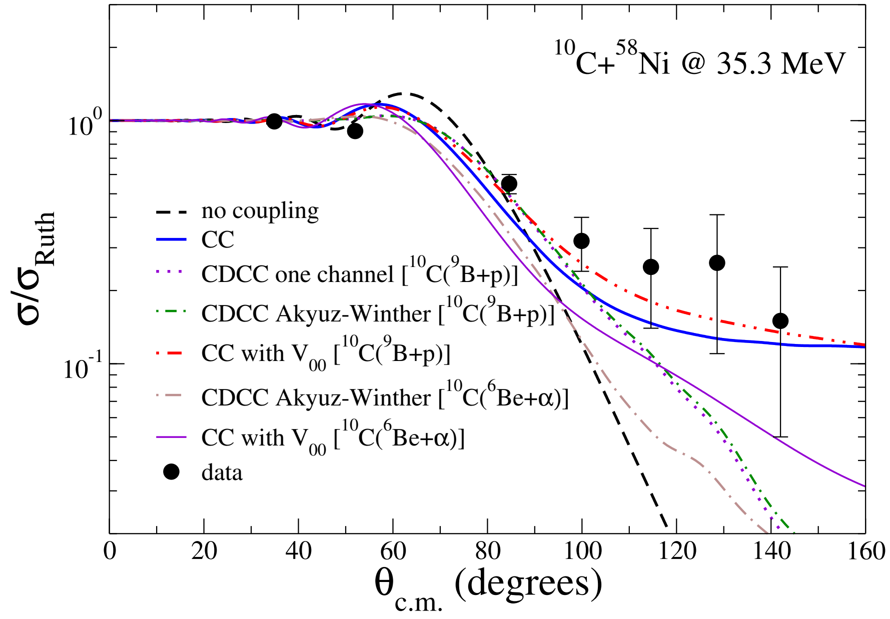

FIG. 10: Elastic scattering angular distribution for the ^{10}C+^{58}Ni system at $E_{\rm Lab}$=35.3 MeV. The curves are results of CC and CDCC calculations.